



Visible light activation of persulfate by magnetic hydrochar for bacterial inactivation: Efficiency, recyclability and mechanisms

Wanjun Wang, Hanna Wang, Guiying Li, Po Keung Wong, Taicheng An*

Guangdong Key Laboratory of Environmental Catalysis and Health Risk Control, School of Environmental Science and Engineering, Institute of Environmental Health and Pollution Control, Guangdong University of Technology, Guangzhou, China

ARTICLE INFO

Article history:

Received 27 December 2019

Received in revised form

9 March 2020

Accepted 20 March 2020

Available online 22 March 2020

Keywords:

Bacterial inactivation

Photocatalysis

Persulfate activation

Visible light

Magnetic hydrochar

ABSTRACT

The development of “green” water disinfection technology utilizing solar energy is highly desired but remains challenging. In this study, sulfate radical ($\bullet\text{SO}_4^-$)-mediated bacterial inactivation was first attempted by using Fe_3O_4 -based magnetic hydrochar (MHC) as a recyclable catalyst for persulfate (PS) activation under visible light (VL) irradiation. Complete treatment of 8.0 log *E. coli* cells was reached within 40 min in VL/PS/MHC system, compared with that of only 2.0 log-reduction was obtained in the PS/MHC system under the same conditions. The system was applicable in wide range of pH (3.0–9.0), and increasing dissolved O_2 could further promote the efficiency. A three-route mechanism was proposed, in which the PS activation by $\equiv\text{Fe}(\text{II})$ of Fe_3O_4 and photo-generated electron captured by PS were the major processes. The bacterial cell lesion process was found to be triggered directly via $\bullet\text{SO}_4^-$, which caused the damage of outer membrane, followed by up-regulation of intracellular ROSs and destroy of chromosomal DNA, finally leading to irreversible cell death. Moreover, the VL/PS/MHC system is also effective to inactivate versatile pathogenic bacteria including *P. aeruginosa* and *S. aureus*. As a proof-of-concept, our study provides meaningful information to advance the areas of “green” water disinfection technology which can be realized by recyclable photocatalytic systems using solar energy.

© 2020 Elsevier Ltd. All rights reserved.

1. Introduction

Pathogenic microorganisms transmitted via drinking water have been recognized as the major sources causing waterborne diseases and deaths in developing world (Li et al., 2008). With rapid urbanization of society, there is an increasing microbial contaminated wastewater generation, which leads to outbreaks of waterborne diseases occurring at high level (Ashbolt, 2004). Therefore, effective elimination of pathogens in drinking water is crucial and this calls for efficient disinfection technologies. Although conventional water disinfection technologies, like ozonation, chlorination, and UV, have been extensively used, there are growing concerns about their adverse effects, including carcinogenic disinfection by products, high energy input and bacterial re-colonization (Dalrymple et al., 2010; Wang et al., 2015). Developing alternative “green” and cost-effective disinfection technologies with low energy consumption and high efficiency is urgent, but still challengeable in scientific community (An et al., 2016; You et al., 2019).

Solar disinfection (SODIS) uses the inexhaustible solar energy to

eliminate pathogens in water, which has been practiced as low-cost disinfection method in ancient cultures for centuries. It has been recently emphasized by United Nations (UN) as a “sustainable” and “transferrable” technology, which needs preferential development as alternative for chlorination (Keane et al., 2014). However, the major challenge of SODIS technology remains the low efficiency, and the treated water volume is small (Keane et al., 2014; McGuigan et al., 2012). In this regard, photocatalytic disinfection have received enormous attention as it uses a photocatalyst to accelerate the SODIS process, which can remarkably promote the disinfection efficiency (Ganguly et al., 2018; Li et al. 2015, 2019; Wang et al., 2017). However, the identified photocatalysts are mostly UV responsive, which is ineffective to use the whole solar spectrum. Although a number of excellent visible light (VL) driven photocatalysts have been developed for bacterial inactivation, noble metals (i.e. Pt, Ag) are often loaded as co-catalysts (Feng et al., 2018; Ma et al., 2016; Zhang et al., 2010), and these powdery photocatalysts suffer from difficulties in recovery from aqueous environment (Wang et al., 2018b).

Photo-Fenton-like processes (e.g. $\text{H}_2\text{O}_2/\text{UV}$, persulfate/UV, peroxymonosulfate/UV) have attracted increasing attention for their use in organic pollutants degradation (Pablos et al., 2013; Rehman et al., 2018; Wu et al., 2017), in which the UVC/persulfate (PS)

* Corresponding author.

E-mail address: antc99@gdut.edu.cn (T. An).

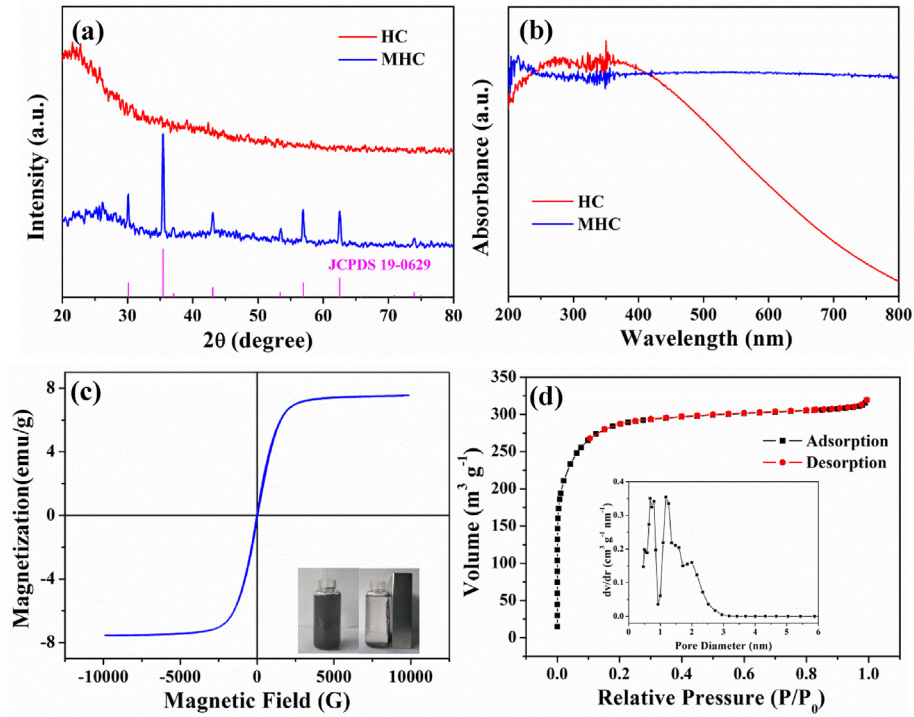


Fig. 1. (a) XRD pattern of the as-prepared hydrochar (HC) and magnetic hydrochar (MHC); (b) UV-Vis DRS spectra of the HC and MHC; (c) Magnetic hysteresis loops of MHC; (d) N_2 adsorption-desorption isotherms of MHC (Inset: pore distribution curve).

system has been promising for *E. coli* inactivation (Michael-Kordatou et al., 2015). Unfortunately, these systems also used UV as the light source to catalyze PS decomposition. Fortunately, we have recently found that PS can also be sensitized with VL

irradiation for *E. coli* elimination (Wang et al., 2019). However, the efficiency of bacterial inactivation is yet not satisfactory for practical use, thus additional technologies are needed to accelerate the PS decomposition process. Generally, transition metal-based

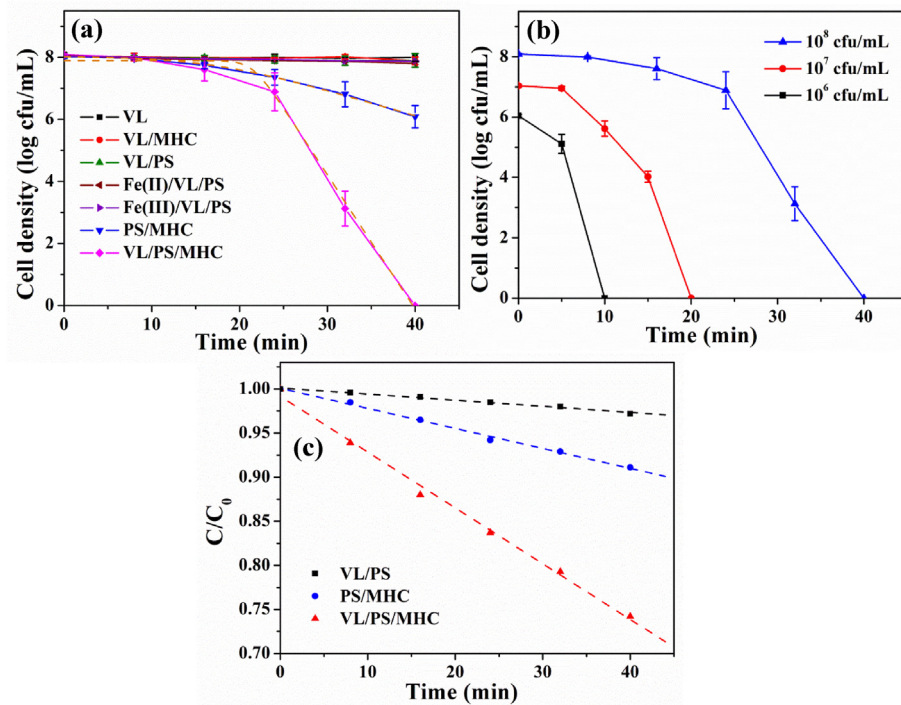


Fig. 2. (a) Bacterial inactivation efficiency in VL/PS/MHC system and other control systems including VL/MHC, VL/PS, Fe/VL/PS and PS/MHC (dash line is kinetic fitting using log-linear-shoulder model); (b) Bacterial inactivation efficiency in VL/PS/MHC system with different initial cell concentrations; (c) PS decomposition kinetics in the VL/PS, PS/MHC and VL/PS/MHC system. Experimental conditions: [MHC] = 200 mg/L; [PS] = 2 mM; [Fe(II)] = 1.5 mg/L; [Fe(III)] = 1.5 mg/L; T = 25 °C; [pH]₀ = 6.0; $\lambda > 420$ nm.

catalysts (Liu et al., 2019a; Waclawek et al., 2017; Wu et al., 2019) and metal-free carbon-based materials (Duan et al. 2015, 2016; Olmez-Hanci et al., 2018) can be applied to activate PS without light irradiation. In addition, it is reported that photo-generated electrons from semiconductor photocatalysts can also be used to promote PS decomposition (Gao et al., 2017). In turn, the electron trapping by PS can suppress the undesired electrons-hole recombination. However, the possible synergistic effect of catalytic PS activation and photocatalysis has not been well studied for bacterial inactivation. Therefore, it is attractive to develop green catalysts that can catalyze the PS decomposition and can also be served as a photocatalyst for bacterial inactivation. The ideal photocatalysts should also be environmental benign, active under VL irradiation as well as facile recycling.

One of such choice is magnetite (Fe_3O_4), which is widely used in constructing composite catalysts with magnetic separable ability. Owing to its small band gap ($E_g = 0.1 \text{ eV}$) (Zhang et al., 2009), it has high VL absorption, but its photocatalytic activity is restrained by fast electron-hole recombination. On the other hand, Fe_3O_4 is also an excellent heterogeneous catalysts to activate PS for degradation of pollutants (Du et al., 2019). However, Fe_3O_4 nanoparticles suffer from aggregation in aqueous solution, leading to decreased catalytic and magnetic properties. One solution is to load the magnetic particles to carbonous materials to prevent particle aggregation (Liu et al., 2019b; Zhu et al. 2014, 2016). In this regard, biochar produced from waste biomass either by pyrolysis (pyrochar) or by hydrothermal carbonization (hydrochar) has received growing interests as absorbents and catalysts supports (Kambo and Dutta, 2015; Qin et al., 2018). Chen et al., (2017) has found that compared with porochar, hydrochar possesses more oxygen functional groups, making it preferable for being utilized as catalyst supports. However, the use of magnetic hydrochar as dual-functional catalyst for PS activation and photocatalysis to inactivate bacteria in water has not been studied yet. Its underlying inactivation mechanisms are also by far understandable.

Herein, magnetic hydrochar was fabricated using a one-step hydrothermal method. The physicochemical properties of the as-prepared sample were characterized by multiple technologies. The bacterial inactivation performances in the presence of magnetic hydrochar and PS were studied in detail under VL irradiation. Moreover, the mechanisms of bacterial inactivation in terms of main reactive species, cell morphology change, antioxidant enzyme activity and chromosomal DNA destruction were all systematically investigated. Furthermore, the universality of this system to inactivate two more pathogenic bacteria was also investigated. This work may provide innovative information to develop low-cost magnetic hydrochar catalysts for recyclable bacterial inactivation under VL, thus finally accomplishing the aim of "green" water disinfection technology using inexhaustible solar energy.

2. Experimental

2.1. Synthesis of materials

Hydrochar (HC) was synthesized via a hydrothermal carbonization process. Briefly, 8.0 g glucose (Aladdin, AR grade) was put into a beaker, followed by adding 80 mL distilled water. Then, the obtained solution in autoclave was subjected to hydrothermal treatment for 10 h at 180 °C. After reaction, the precipitates of HC were collected by centrifugation, washing and drying in vacuum at 60 °C for 24 h before use.

Magnetic hydrochar (MHC) were produced by a modified method using FeCl_3 as precursor of magnetic particles and ZnCl_2 as porogen (Zhu et al., 2014). Typically, 1.0 g anhydrous FeCl_3 (Aladdin, AR grade) and 2.0 g ZnCl_2 (Aladdin, AR grade) were mixed in

12.5 mL distilled water. Then, 2.0 g HC were added to the solution. The mixtures were vigorously stirred for 24 h and then dried for 4 h at 80 °C in air. The dried products were then activated at 600 °C for 90 min in N_2 flow of 1 L min^{-1} . The final products of MHC were washed with 0.1 M HCl, ethanol and water several times before drying for 4 h at 80 °C. The characterization details of the samples were provided in Supporting Information.

2.2. Experiments for bacterial inactivation and analysis

The bacterial inactivation capability of the MHC with PS under VL irradiation were tested using *E. coli* as the model bacteria. The bacterial culture and testing procedures can be found in our previous study (Wang et al., 2019). Briefly, 20 mg MHC was put into 100 mL bacterial cell solution in a flask under vigorous stirring, followed by adding PS (2 mM) under VL irradiation to start the reaction. Two other pathogenic bacterial strains (i.e. *Pseudomonas aeruginosa*, *Staphylococcus aureus*) were also utilized for the testing. The details for analytical methods can be found in Supporting Information.

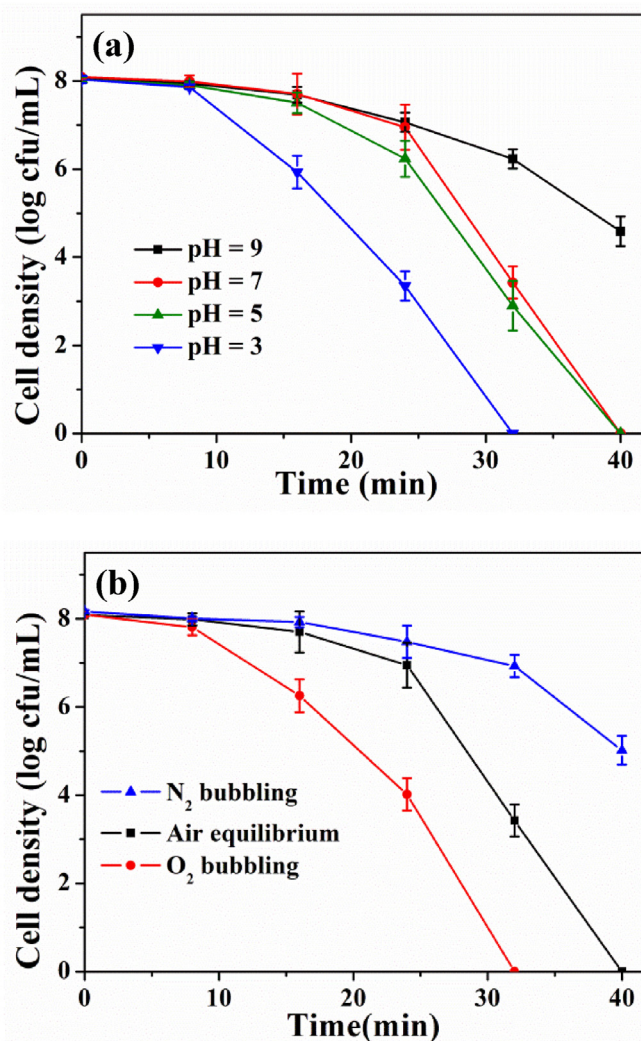


Fig. 3. (a) Effect of different pH on the bacterial inactivation efficiency; (b) Effect of different aeration conditions on the bacterial inactivation efficiency in VL/PS/MHC system. Experimental conditions: [Cell] = 8.0 log cfu/mL; [MHC] = 200 mg/L; [PS] = 2 mM; T = 25 °C; $\lambda > 420 \text{ nm}$.

3. Results and discussion

3.1. Characterization of catalysts

In this study, hydrochar was produced by hydrothermal methods according to previous study (Hu et al., 2017). Then, magnetic particles were incorporated into the hydrochar by pre-impregnation with iron salts, followed by thermal activation. As shown in Fig. 1a, the XRD of the samples show that the pure hydrochar (HC) is amorphous in nature, as there is only a broad peak of $20^\circ - 30^\circ$ corresponding to graphite. In contrast, the obtained magnetic hydrochar (MHC) shows strong diffraction peaks at 30.1° , 35.4° , 56.9° , 43.1° and 62.5° , which can be assigned to crystal planes of Fe_3O_4 in cubic phase (JCPDS 19–0629, space group: Fd3m), suggesting Fe_3O_4 nanoparticles are successfully fabricated onto HC without other impurities. The UV–Vis absorption spectra show that the pristine HC exhibits semiconductor-like absorption with cutoff wavelength up to 800 nm (Fig. 1b), which is due to delocalized π electrons in HC (Hu et al., 2017). After incorporation with Fe_3O_4 , the MHC exhibits obviously enhanced VL absorption because of the narrow band gap of Fe_3O_4 ($E_g = 0.1$ eV) (Zhang et al., 2009). The magnetization curve in Fig. 1c indicates the MHC has superparamagnetic property with zero resonance and coercivity. The saturated magnetization value of MHC reached 7.5 emu/g. Such superparamagnetic property favors the rapid separation of the catalysts from aqueous solution (Qin et al., 2015). As demonstrated in the inset of Fig. 1c, the MHC powders can be tightly attracted on the vessel by external magnet, suggesting its good magnetic recyclability. The Fe_3O_4 weight ratio determined by ICP-OES was 9.17% in the MHC composites.

The N_2 adsorption–desorption isotherm of MHC shown in Fig. 1d demonstrates a type-I isotherm with microporous structure (Kyotani et al., 2003). The pore sized distribution (inset of Fig. 1d) confirms the microporosity with pore size below 3 nm. As shown in

Table S1, the degree of microporosity demonstrated by the ratio of micropore volume/total volume (V_{mic}/V_t) was calculated to be 81.4%. The surface area (BET) was obtained as over 1072 m^2/g (1356 m^2/g when using Langmuir model). In contrast, the pristine HC shows a type-IV isotherm with hysteresis loop (Fig. S1), indicating a mesoporous structure. The proportion of microporosity decreased to be 1%, and the BET surface area was only 9.18 m^2/g (Table S1). The remarkably increased surface area and microporosity on MHC would be benefit for PS absorption, thus promoting subsequent PS decomposition and bacterial inactivation efficiencies.

The morphology of MHC was analyzed using TEM and SEM (Fig. S2). A typical SEM image of the as-prepared MHC exhibits microsphere morphology with particle diameters of 200–400 nm. The spherical morphology is not changed, suggesting Fe_3O_4 loading would not change the microstructure of HC. The TEM image clearly demonstrates that Fe_3O_4 with sizes of 20–50 nm were anchored on the amorphous carbon sphere. In addition, the HRTEM further shows clear crystal lattice fringe with interplanar distance to be 0.253 nm, which corresponds to the (311) crystal plane of Fe_3O_4 . The HAADF-STEM image and corresponding EDX elemental mapping at the atomic scale further confirms the existence of C, O, and Fe elements. The surface Fe content was determined to be 12.7%. These results confirm the successful synthesis of Fe_3O_4 loaded hydrochar with large surface area and high porosity.

3.2. Bacterial inactivation efficiency

As a microbiological indicator in drinking water, *E. coli* was used to test the catalytic inactivation activity of the MHC sample. To test the applicability in heavily microbial contaminated water, a relative high cell concentration of 10^8 cfu/mL was applied hereafter. As Fig. 2a shows, with VL/PS or VL/MHC, almost no bacterial inactivation efficiency was observed, suggesting PS activation by VL

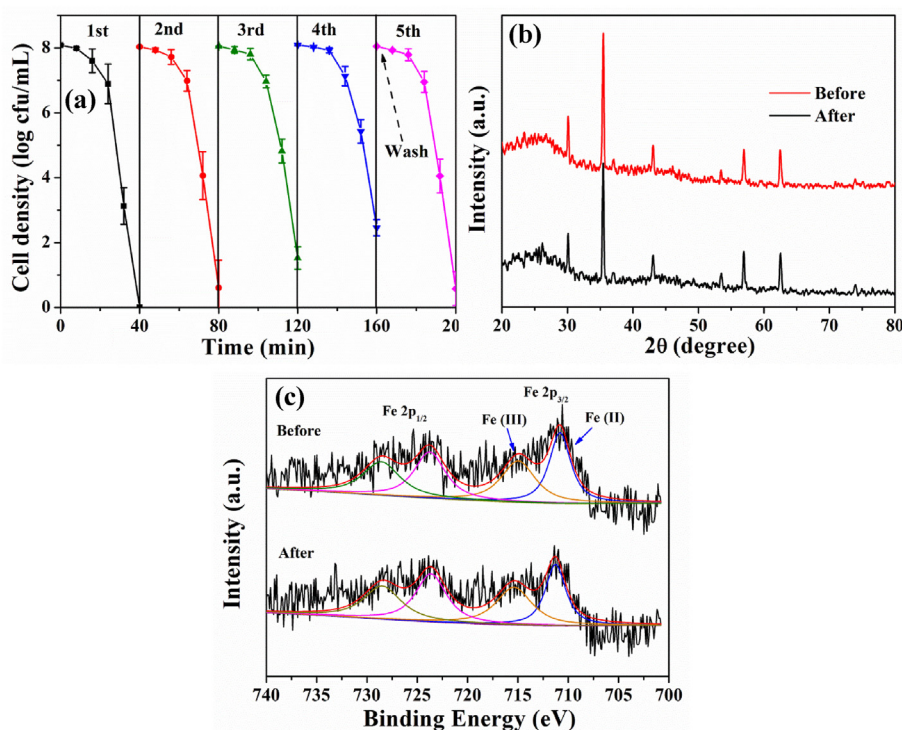


Fig. 4. (a) Repeated experiments for bacterial inactivation in the VL/PS/MHC system; (b) XRD patterns and (c) High-resolution Fe 2p XPS spectra of MHC sample before and after the reaction. Experimental conditions: [Cell] = 8.0 log cfu/mL; [MHC] = 200 mg/L; [PS] = 2 mM; $T = 25$ $^\circ\text{C}$; $[\text{pH}]_0 = 6.0$; $\lambda > 420$ nm.

alone and photocatalytic activity of MHC by VL alone are not effective for high concentration bacterial inactivation, although we have previously found that the VL/PS system can inactivate bacterial cells with much lower concentration of 10^7 cfu/mL within 120 min (Wang et al., 2019). In case of PS/MHC, it was found that about 2.0 log-reduction of *E. coli* cells was inactivated after 40 min, suggesting that the PS could be activated by Fe_3O_4 loaded into MHC to cause moderate cell inactivation. Interestingly, in VL/PS/MHC system, the bacterial inactivation efficiency was remarkably enhanced and complete inactivation of 8 log viable cells was accomplished within 40 min. The bacterial inactivation kinetic was studied according to the log-linear-shoulder model (Geeraerd et al., 2005). The obtained specific inactivation rate constant k_{\max} ($R^2 = 0.99$) was calculated to be 0.19 and 0.99 min^{-1} for bacterial inactivation in the PS/MHC and VL/PS/MHC system, respectively. Therefore, the bacterial inactivation efficiency by the VL/PS/MHC system is about 5.21 times higher than that of PS/MHC system. In addition, when the concentration of cells was decreased to normal levels of 10^7 and 10^6 cfu/mL, the complete inactivation was achieved within 20 min and 10 min, respectively (Fig. 2b). It should be noted that this bacterial inactivation efficiency exceeds most of the VL-driven photocatalytic systems reported so far, except some Ag-based photocatalysts (Table S2). Since the possible released Ag is toxic to environment and would cause secondary pollution, thus the MHC is more environmental benign and low cost which shows promise for large scale applications.

The PS decomposition kinetics was studied according to first-order kinetics' model (Fig. 2c). The obtained apparent reaction constant (k) ($R^2 = 0.99$) was 6.32×10^{-3} , 2.27×10^{-3} and $6.93 \times 10^{-4} \text{ min}^{-1}$ for VL/PS/MHC, PS/MHC and VL/PS system, respectively. It is clear that the VL/PS/MHC system exhibits the highest PS decomposition efficiency, which matches well with the above bacterial inactivation efficiency. The PS concentration was decreased from 2 mM to 1.484 mM after completed 40 min reaction, which indicates that 0.516 mM PS was decomposed, corresponding to a SO_4^{2-} release concentration of 99.1 mg/L theoretically. This value was significantly lower than the pollution limit of SO_4^{2-} (250 mg/L) in drinking water suggested by the World Health Organization (WHO) (Ioannidi et al., 2018). Therefore, the released SO_4^{2-} concentration is low and would not cause significant secondary pollution. The possible released Fe content was also measured to be only about 1.31 mg/L after completed 40 min reaction (Fig. S3). The addition of equivalent amount of Fe^{2+} (1.5 mg/L) or Fe^{3+} (1.5 mg/L) in the VL/PS system without catalysts would not cause significant bacterial inactivation (Fig. 2a). Therefore, the homogeneous reaction by $\text{Fe}/\text{VL}/\text{PS}$ could be excluded, due to the low amount of Fe ions which cannot trigger sufficient ROSs to cause bacterial inactivation.

The effect of pH on bacterial inactivation efficiency was studied (Fig. 3a). The control experiments show that the pH variation in the range of 3.0–9.0 will not cause obvious bacterial inactivation, suggesting pH value alone has negligible effect on the inactivation efficiency in the test period (Fig. S4). The pH variation in the VL/PS/MHC system was monitored, which shows that all the pH values are decreased a little under different initial pH, and the pH is decreased more significantly under alkaline condition (Fig. S5a). Generally, it is known that basic pH could accelerate PS decomposition to produce $\bullet\text{OH}$, thus enhancing the degradation efficiency towards organic pollutants (Furman et al., 2010). Nevertheless, in the present work, it was recognized that when pH value was increased to 9.0, only about 3.0 log reduction of viable cells was found in 40 min of treatment. In contrast, when the pH was decreased to 3.0, total inactivation of 8.0 log cells could be completed within 30 min, suggesting acidic pH would favor the disinfection activity (Fig. 3a). This can be partially due to the fact that the surface of *E. coli* cells is

negatively charged, which results in the electrostatic repulsion between the cells and $\text{S}_2\text{O}_8^{2-}$. The adsorption of PS onto the cells is hindered with higher pH value, thus reducing the bacterial inactivation activity. Nevertheless, compared with traditional homogeneous photo-Fenton methods in which only strong acidic pH can be applied, the VL/PS/MHC system can be applied in a wide pH range of 3.0–9.0 for water disinfection.

The effect of dissolved O_2 on the disinfection efficiency was investigated by pumping with O_2 or N_2 in the reaction mixture. As shown in Figs. 3b and 8.0 log reduction of *E. coli* cells is reached within 30 min, which is much faster than that of normal air equilibrium conditions, indicating dissolved O_2 is crucial to obtain high inactivation efficiency. This was further confirmed by N_2 bubbling experiments that N_2 bubbling was found to significantly inhibit the bacterial inactivation process. The pH variation was also monitored, which shows that the pH is decreased more significantly with O_2 bubbling (Fig. S5b). It has been reported the $\text{Fe}(\text{II})$ could reduce dissolved molecular O_2 to produce H_2O_2 via generation of $\bullet\text{O}_2^-$ (Eqs. (1) and (2)) (Harrington et al., 2012), which can further promote the PS decomposition to generate $\bullet\text{SO}_4^-$ (Eqs. (3) and (4)) (Zhang et al., 2017). To support this conclusion, the generation of H_2O_2 was

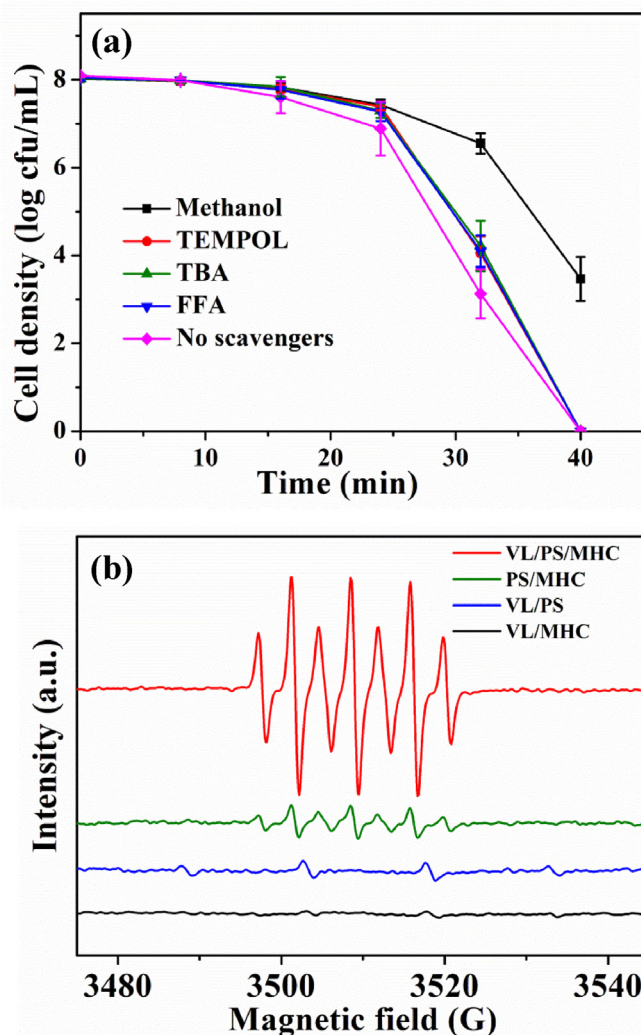


Fig. 5. (a) Bacterial inactivation efficiency in VL/PS/MHC system with different scavengers (1 mM methanol, TEMPOL, TBA and FFA). (b) EPR spectra of DMPO spin-trapping adducts in different systems. Experimental conditions: $[\text{Cell}] = 8.0 \text{ log cfu/mL}$; $[\text{MHC}] = 200 \text{ mg/L}$; $[\text{PS}] = 2 \text{ mM}$; $T = 25 \text{ }^\circ\text{C}$; $[\text{pH}]_0 = 6.0$; $\lambda > 420 \text{ nm}$.

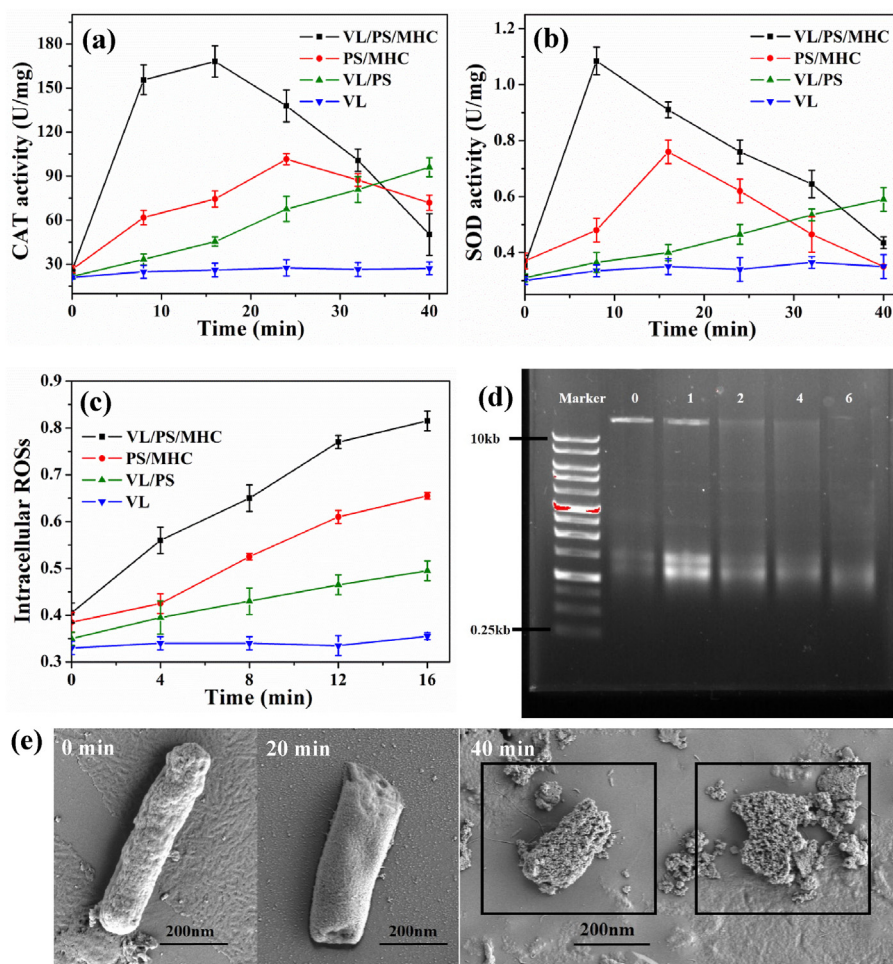
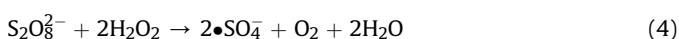
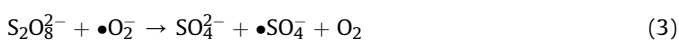
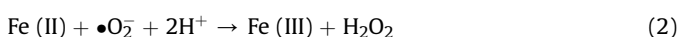


Fig. 6. (a) CAT activity; (b) SOD activity and (c) Intracellular ROSs levels of bacteria in different treatment systems; (d) DNA agarose gel electrophoresis of bacterial cells in the VL/PS/MHC system; (e) SEM images of *E. coli* cell treated by the VL/PS/MHC system with different irradiation time. Experimental conditions: [Cell] = 8.0 log cfu/mL; [MHC] = 200 mg/L; [PS] = 2 mM; T = 25 °C; [pH]₀ = 6.0; λ > 420 nm.

monitored (Fig. S6). Results evidenced that the H₂O₂ was produced with reaction time, and the concentrations followed the order of O₂ bubbling (6.36 μM) > air equilibrium (4.85 μM) > N₂ bubbling (2.88 μM). Therefore, increasing dissolved O₂ could promote H₂O₂ generation, leading to acceleration of PS decomposition and enhanced bacterial inactivation efficiency. In addition, the increased dissolved O₂ was also supposed to trap the photo-generated electrons, thus preventing the undesired charge recombination on MHC photocatalysts, which further improving the disinfection efficiency.



The reusability and regeneration of photocatalyst is vital for practical applications. To test the recyclability, the used photocatalysts were simply recovered by external magnetic field. The treated effluent was drawn out, followed by directly adding another set of bacterial suspension with cell concentrations of 8.0 log cfu/mL. As demonstrated in Fig. 4a, in the first run, all of the bacterial

cells were inactivated within 40 min of VL irradiation. Generally, the bacterial inactivation efficiency remains stable in the repeated experiments, while slightly decreases in the 3rd and 4th run. The bacterial inactivation efficiency could still reach more than 5.0 log reduction in the 4th run (corresponding to 99.999% disinfection efficiency). In addition, the efficiency was found to be completely recovered in the 5th run after the catalyst was regenerated simply by washing with distill water (Fig. 4a), suggesting the MHC can be reused without activity deterioration. To evaluate the effect of dark absorption, the dark absorption of the bacteria using the MHC sample after reaction and washing was studied, and compared with the 1st dark absorption before the reaction. The results indicated that the dark absorption of the bacteria was low, and there was no significant difference between the 1st dark absorption and 2nd dark absorption (Fig. S7), suggesting the recovery of the bacterial inactivation efficiency was not due to dark absorption.

Moreover, the XRD before and after the reactions illustrated in Fig. 4b demonstrates there is no detectable crystal structure change of the MHC sample. In addition, XPS of the Fe spectrum clearly shows the co-exists of Fe(II) and Fe(III). The bind energy peak located at 710.8 and 723.8 eV can be assigned to Fe(II), while the bind energy peak located at 715.0 and 728.0 eV can be attributed to Fe(III), respectively (Fig. 4c). It is found that the surface contents of Fe(II)/Fe(III) decreases slightly from 51.8/48.2 to 48.3/51.7 after the reaction, suggesting only limited amount of surface Fe(II) is

oxidized to Fe(III) during the reaction. This results further confirms the high photo-stability and recyclability, which is essential for low-cost applications.

3.3. Bacterial inactivation mechanism

The possible main reactive species in the system of PS/VL/MHC were investigated by using specific scavengers to trap potential reactive species. Methanol, *tert*-butyl alcohol (TBA), furfuryl alcohol (FFA) and TEMPOL were applied as scavengers for $\bullet\text{SO}_4^-$, $\bullet\text{OH}$, $^1\text{O}_2$ and $\bullet\text{O}_2^-$, respectively (Wang et al., 2011; Xia et al., 2018). As Fig. 5a shows, with the addition of 1 mM TBA, FFA, and TEMPOL, there is no obvious effect on the bacterial inactivation efficiency, suggesting that $\bullet\text{OH}$, $^1\text{O}_2$ and $\bullet\text{O}_2^-$ were not the main species during the bacterial inactivation process. Methanol is known to trap both $\bullet\text{OH}$ and $\bullet\text{SO}_4^-$ radicals (Rastogi et al., 2009). The addition of methanol was found to significantly inhibit the cell inactivation efficiency, indicating that the main species is $\bullet\text{SO}_4^-$. To further confirm the dominant role of $\bullet\text{SO}_4^-$, EPR characterization using DMPO as spin trapping reagent was conducted to distinguish different radicals (Cai et al., 2019). As Fig. 5b shows, the EPR spectra with seven main peaks can be assigned to DMPOX adduct, which was originated from the oxidation of DMPO by $\bullet\text{SO}_4^-$, as the $\bullet\text{SO}_4^-$ /DMPO adduct is reported to be not stable and would be transformed to DMPOX immediately (Du et al., 2019). In addition, the ESR signal of DMPOX was also found in PS/MHC system with much smaller intensity, suggesting the $\bullet\text{SO}_4^-$ was also the major reactive species but the $\bullet\text{SO}_4^-$ concentration was significant smaller than that in VL/PS/MHC system, which is consistent with the above cell inactivation performances (Fig. 2a). However, in the cases of VL/PS and VL/MHC, only weak signals of DMPO/ $\bullet\text{OH}$ was observed. Since the $\bullet\text{SO}_4^-$ will further transform to $\bullet\text{OH}$ (Ahmad et al., 2013), this result indicates only small amount of $\bullet\text{SO}_4^-$ was produced and immediately annihilated to produce trace amount of $\bullet\text{OH}$, resulting in low cell inactivation ratio in VL/PS and VL/MHC systems. All these confirm that the main active species for the VL/PS/MHC is $\bullet\text{SO}_4^-$ rather than $\bullet\text{OH}$. Large amounts of $\bullet\text{SO}_4^-$ is produced and directly cause the loss

of bacterial cells viability.

To further investigate the cell lesions mechanism caused by $\bullet\text{SO}_4^-$, several intracellular enzymatic activities were also analyzed during the treatment process. Catalase (CAT) is a typical enzyme which catalyze the decomposition of H_2O_2 . It is found in Fig. 6a that the CAT level increases promptly in the first 10 min and reaches the highest value in 15 min, and then decreases gradually with the complete of bacterial inactivation. This indicates the bacterial cells were encountering significant oxidative stress, and high level of enzyme was induced to annihilate the ROSs, leading to the slow bacterial inactivation rate at the initial stage. After the bacterial defending system was overwhelmed by continuous ROSs attacking, the cell apoptosis occurred. Compared with the VL/PS/MHC system, the induced CAT level was much lower in the VL/PS and PS/MHC system, suggesting the reduced oxidative stress in the systems which results in low inactivation efficiency. Similar phenomenon was also observed in the case of superoxide dismutase (SOD) activity (Fig. 6b). These results indicate the attacking of $\bullet\text{SO}_4^-$ is associated with up-regulation of intracellular ROSs including H_2O_2 , $\bullet\text{O}_2^-$ and $\bullet\text{OH}$, which can initiate the chain oxidation reaction inside cell as reported in previous studies (Sun et al., 2014). To further confirm this conclusion, total intracellular ROSs was also examined using fluorescent probe DCFH-DA (Fig. 6c). The intracellular ROS level increased with time, and intensity on VL/PS/MHC system was the highest, suggesting the oxidation process is like a self-propagating progress induced by up-regulation of intracellular ROSs. The intracellular ROSs would then lead to the cytoplasm oxidation and destruction of genomic DNA (Fig. 6d), finally resulting in the irreversible cell death.

To test the bacterial re-growth activity, the cell lesions process was also examined by SEM observation. As indicated in Fig. 6e, the cell structure was intact at the initial stage, while the cell outer membrane was ruptured and lots of holes were observed after 10 min of VL irradiation, suggesting the first attacking site by $\bullet\text{SO}_4^-$ is the cell membrane, which is consistent with $\bullet\text{OH}$ -mediated disinfection process (Chen et al., 2019; Liang et al., 2018; Wang et al., 2018a). With prolonged reaction time, the cell was

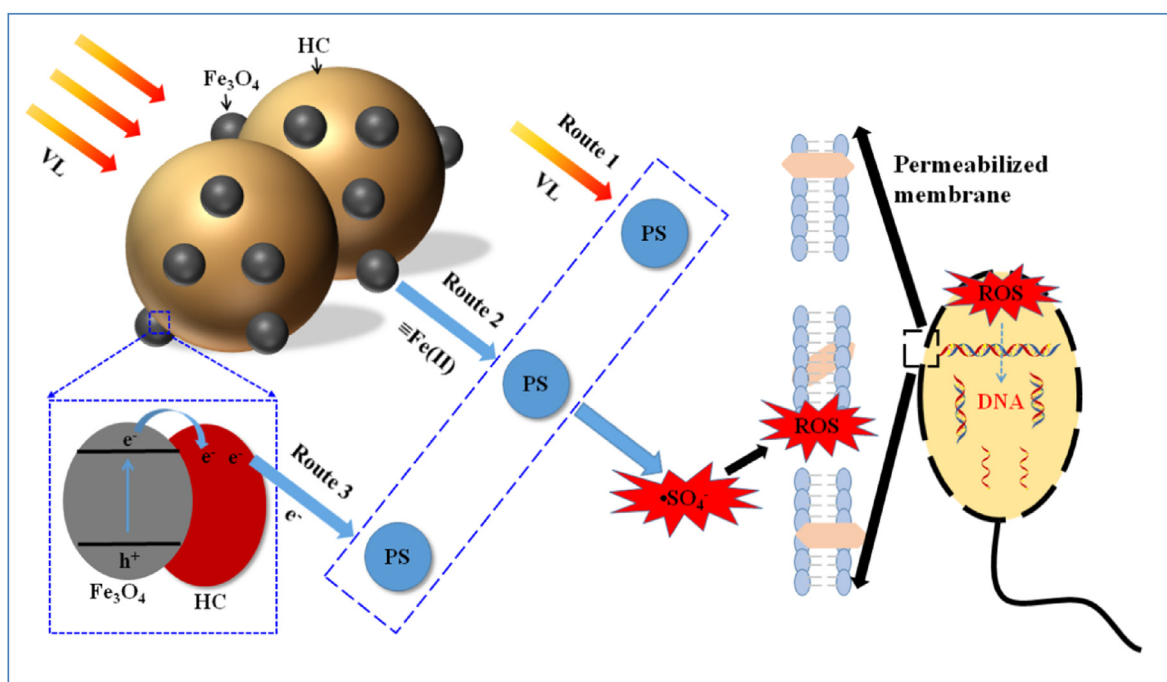
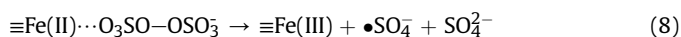
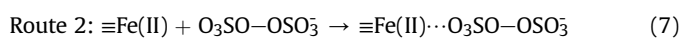
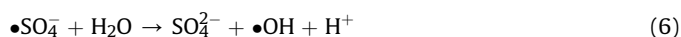


Fig. 7. Schematic illustration of the bacterial inactivation mechanism in the VL/PS/MHC system.

completely destroyed, leaving only cell debris after 40 min. Therefore, there is no bacterial re-colonization after dark repair, since the cell structure is oxidized into pieces. The released organic bio-molecules would then be further oxidized and mineralized, as confirmed by TOC analysis (Fig. S8). The bulk TOC was increased at the initial stage, due to the release of intracellular components, and then decreased gradually, suggesting the subsequent elimination of the released organics.

Based on the above results, a tentative mechanism of the bacterial inactivation was proposed in Fig. 7. When MHC was irradiated by VL in the presence of PS, three major processes were occurred: (1) the PS was directly sensitized by VL to generate $\bullet\text{SO}_4^-$, which subsequently transformed to $\bullet\text{OH}$ (Eqs. (5) and (6)), as confirmed in Fig. 5b and also evidenced in our prior study (Wang et al., 2019); (2) the surface or lattice Fe(II) in Fe_3O_4 could absorb PS to form $\equiv\text{Fe(II)}/\text{O}_3\text{SO}-\text{OSO}_3^-$ complex (Xia et al., 2018), which then trigger the homolytic dissociation of O–O bonds in PS and then produce $\equiv\text{Fe(III)}$ and $\bullet\text{SO}_4^-$ (Eqs. (7) and (8)). This route is supported by the moderate bacterial inactivation activity in PS/MHC system (Fig. 2a); (3) the photo-excitation of Fe_3O_4 generated photo-electrons on the conduction band (CB) of the photocatalysts (Eq. (9)). The CB electrons then transfer to the adsorbed PS, and lead to the sensitization of PS to generate $\bullet\text{SO}_4^-$ (Eq. (10)). The CB electron trapping by PS could further promote the separation of electron-hole recombination, thus increasing the quantum efficiency of photocatalysis. The three route reactions occurred simultaneously in which the latter two are more important, exhibiting a synergistic effect. It is noted that in normal photocatalytic reaction process, the CB electrons could be captured by O_2 to generate $\bullet\text{O}_2^-$ (Ribao et al., 2019). However, in the PS-mediated photocatalytic process, the CB electrons were captured more efficiently by PS rather than O_2 , as evidenced in Fig. 5a that the TEMPOL (a $\bullet\text{O}_2^-$ scavenger) has no effect on the bacterial inactivation performance. Therefore, the main species in VL/PS/MHC system is assumed as $\bullet\text{SO}_4^-$, which cause the cell membrane oxidation and trigger chain reactions including up-regulation of intracellular ROSs, finally leading to the cell death.



3.4. Versatility for water disinfection

One major concern to develop novel water disinfection technology is the feasibility for pathogenic microorganism inactivation. However, most of the previous studies only used one model bacterium such as *E. coli* to characterize the water disinfection activity (He et al., 2019). To further test the versatility of using VL/PS/MHC system for water disinfection, several other pathogenic bacterial strains were also used as the targets. *Staphylococcus aureus* (*S. aureus*) is a pathogen causing skin infections and food-borne disease, while *Pseudomonas aeruginosa* (*P. aeruginosa*) is a pathogen with multidrug resistance which is responsible for hospital-acquired infections (HAI). Fig. 8 shows the cell inactivation rate towards *P. aeruginosa* and *S. aureus* in the PS/VL/MHC system. For

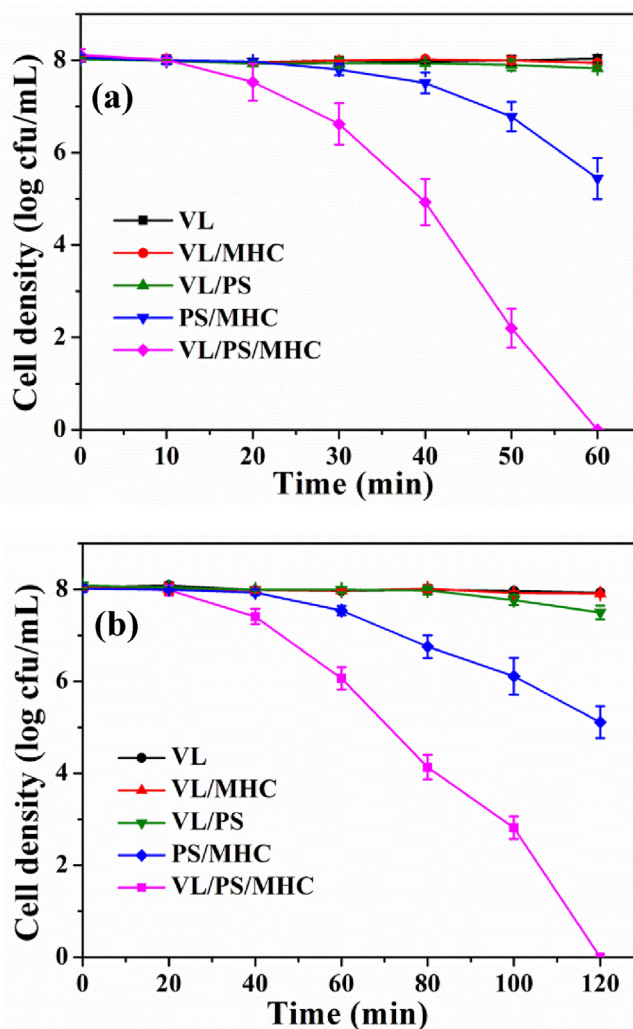


Fig. 8. Bacterial inactivation efficiency for (a) *P. aeruginosa* and (b) *S. aureus* by the VL/PS/MHC system. Experimental conditions: [Cell] = 8.0 log cfu/mL; [MHC] = 200 mg/L; [PS] = 2 mM; T = 25 °C; [pH]₀ = 6.0; λ > 420 nm.

P. aeruginosa, total inactivation of 8 log cells was reached after 90 min, which was much longer than that for *E. coli*. For *S. aureus*, the complete inactivation time was extended to 120 min, suggesting that the sensitivity of different bacteria responding to the $\bullet\text{SO}_4^-$ -mediated process follows the order of *S. aureus* < *P. aeruginosa* < *E. coli*. This phenomenon can be partially attributed to the different structure of cell wall of the tested bacteria. As a Gram-positive bacterium, *S. aureus* has much thicker peptidoglycan layer (20–80 nm) than that of Gram-negative bacterium (10 nm) (Chen et al., 2013), which results in higher oxidation resistant to $\bullet\text{SO}_4^-$ attacking. As a Gram-negative bacterium, *P. aeruginosa* possesses multidrug resistant genes, which makes it has higher resistance than Gram-negative *E. coli*. Nevertheless, these results indicate that the present system is effective to inactivate both Gram-negative, Gram-positive as well as drug-resistant pathogenic bacteria, exhibiting prospect for versatile disinfection applications.

4. Conclusions

In this study, magnetic separable hydrochar was synthesized and applied for bacterial inactivation under VL through $\bullet\text{SO}_4^-$ -

mediated processes. Complete inactivation of 8.0 log *E. coli* cells could be achieved after 40 min, and 7.0 log cells could be treated within 20 min, in which the efficiency was much higher than most of the traditional photocatalytic disinfection process. The major reactive species was found to be $\bullet\text{SO}_4^-$ rather than $\bullet\text{OH}$ or $\bullet\text{O}_2^-$, which caused the damage of outer membrane and triggered the up-regulation of intracellular ROSSs. The $\equiv\text{Fe(II)}$ complex in the MHC could catalyze the decomposition of PS, while the photo-generated electrons from MHC could be captured by PS for generating $\bullet\text{SO}_4^-$, which cooperatively promote the PS activation for bacterial inactivation. Moreover, the MHC could be easily recycled and used for universal treatment of pathogenic bacteria including *P. aeruginosa* and *S. aureus*. These results were expected to provide advanced information not only for advancing the areas of water disinfection using recyclable catalysts and solar energy, but also for further studying the cell inactivation mechanism in $\bullet\text{SO}_4^-$ -mediated advanced oxidation processes.

Declaration of competing interest

The authors declare that they have no known competing financial interests or personal relationships that could have appeared to influence the work reported in this paper.

Acknowledgements

This work was supported by the National Natural Science Foundation of China (21607028, 41425015 and U1901210), the Research Grant Council of Hong Kong SAR Government (GRF14100115), Science and Technology Project of Guangdong Province, China (2017A050506049), Local Innovative and Research Teams Project of Guangdong Pearl River Talents Program (2017BT01Z032), and Leading Scientific, Technical and Innovation Talents of Guangdong special support program (2016TX03Z094).

Appendix A. Supplementary data

Supplementary data to this article can be found online at <https://doi.org/10.1016/j.watres.2020.115746>.

References

- Ahmad, M., Teel, A.L., Watts, R.J., 2013. Mechanism of persulfate activation by phenols. *Environ. Sci. Technol.* 47, 5864–5871.
- An, T.C., Zhao, H.J., Wong, P.K., 2016. *Advances in Photocatalytic Disinfection*. Springer-Verlag, Germany.
- Ashbolt, N.J., 2004. Microbial contamination of drinking water and disease outcomes in developing regions. *Toxicology* 198, 229–238.
- Cai, C., Kang, S., Xie, X., Liao, C., 2019. Ultrasound-assisted heterogeneous peroxy-monosulfate activation with Co/SBA-15 for the efficient degradation of organic contaminant in water. *J. Hazard Mater.* 121519.
- Chen, N., Huang, Y.H., Hou, X.J., Ai, Z.H., Zhang, L.Z., 2017. Photochemistry of hydrochar: reactive oxygen species generation and sulfadimidine degradation. *Environ. Sci. Technol.* 51, 11278–11287.
- Chen, Y.F., Tang, X.N., Gao, X., Zhang, B., Luo, Y., Yao, X.Y., 2019. Antimicrobial property and photocatalytic antibacterial mechanism of the TiO₂-doped SiO₂ hybrid materials under ultraviolet-light irradiation and visible-light irradiation. *Ceram. Int.* 45, 15505–15513.
- Chen, Y.M., Ng, T.W., Lu, A.H., Li, Y., Yip, H.Y., An, T.C., Li, G.Y., Zhao, H.J., Gao, M.H., Wong, P.K., 2013. Comparative study of visible-light-driven photocatalytic inactivation of two different wastewater bacteria by natural sphalerite. *Chem. Eng. J.* 234, 43–48.
- Dalrymple, O.K., Stefanakos, E., Trotz, M.A., Goswami, D.Y., 2010. A review of the mechanisms and modeling of photocatalytic disinfection. *Appl. Catal. B Environ.* 98, 27–38.
- Du, J.K., Bao, J.G., Liu, Y., Kim, S.H., Dionysiou, D.D., 2019. Facile preparation of porous Mn/Fe₃O₄ cubes as peroxy-monosulfate activating catalyst for effective bisphenol A degradation. *Chem. Eng. J.* 376, 9.
- Duan, X.G., Sun, H.Q., Kang, J., Wang, Y.X., Indrawirawan, S., Wang, S.B., 2015. Insights into heterogeneous catalysis of persulfate activation on dimensional-structured nanocarbons. *ACS Catal.* 5, 4629–4636.
- Duan, X.G., Ao, Z.M., Zhou, L., Sun, H.Q., Wang, G.X., Wang, S.B., 2016. Occurrence of radical and nonradical pathways from carbocatalysts for aqueous and nonaqueous catalytic oxidation. *Appl. Catal. B Environ.* 188, 98–105.
- Feng, T., Liang, J.L., Ma, Z.Y., Li, M.A., Tong, M.P., 2018. Bactericidal activity and mechanisms of BiOBr-AgBr under both dark and visible light irradiation conditions. *Colloids Surf. B Biointerfaces* 167, 275–283.
- Furman, O.S., Teel, A.L., Watts, R.J., 2010. Mechanism of base activation of persulfate. *Environ. Sci. Technol.* 44, 6423–6428.
- Ganguly, P., Byrne, C., Breen, A., Pillai, S.C., 2018. Antimicrobial activity of photocatalysts: fundamentals, mechanisms, kinetics and recent advances. *Appl. Catal. B Environ.* 225, 51–75.
- Gao, Y.W., Li, S.M., Li, Y.X., Yao, L.Y., Zhang, H., 2017. Accelerated photocatalytic degradation of organic pollutant over metal-organic framework MIL-53(Fe) under visible LED light mediated by persulfate. *Appl. Catal. B Environ.* 202, 165–174.
- Geeraerd, A.H., Valdramidis, V., Van Impe, J.F., 2005. GlnaFIT, a freeware tool to assess non-log-linear microbial survivor curves. *Int. J. Food Microbiol.* 102, 95–105.
- Harrington, A.D., Hylton, S., Schoonen, M.A.A., 2012. Pyrite-driven reactive oxygen species formation in simulated lung fluid: implications for coal workers' pneumoconiosis. *Environ. Geochem. Health* 34, 527–538.
- He, N.N., Cao, S.H., Zhang, L.H., Tian, Z.D., Chen, H., Jiang, F., 2019. Enhanced photocatalytic disinfection of *Escherichia coli* K-12 by porous g-C₃N₄ nanosheets: combined effect of photo-generated and intracellular ROSSs. *Chemosphere* 235, 1116–1124.
- Hu, Z.F., Shen, Z.R., Yu, J.C., 2017. Converting carbohydrates to carbon-based photocatalysts for environmental treatment. *Environ. Sci. Technol.* 51, 7076–7083.
- Ioannidi, A., Frontistis, Z., Mantzavinos, D., 2018. Destruction of propyl paraben by persulfate activated with UV-A light emitting diodes. *J. Environ. Chem. Eng.* 6, 2992–2997.
- Kambo, H.S., Dutta, A., 2015. A comparative review of biochar and hydrochar in terms of production, physico-chemical properties and applications. *Renew. Sustain. Energy Rev.* 45, 359–378.
- Keane, D.A., McGuigan, K.G., Ibanez, P.F., Polo-Lopez, M.I., Byrne, J.A., Dunlop, P.S.M., O'Shea, K., Dionysiou, D.D., Pillai, S.C., 2014. Solar photocatalysis for water disinfection: materials and reactor design. *Catal. Sci. Technol.* 4, 1211–1226.
- Kyotani, T., Ma, Z.X., Tomita, A., 2003. Template synthesis of novel porous carbons using various types of zeolites. *Carbon* 41, 1451–1459.
- Li, G.Y., Nie, X., Chen, J.Y., Jiang, Q., An, T.C., Wong, P.K., Zhang, H.M., Zhao, H.J., Yamashita, H., 2015. Enhanced visible-light-driven photocatalytic inactivation of *Escherichia coli* using g-C₃N₄/TiO₂ hybrid photocatalyst synthesized using a hydrothermal-calcination approach. *Water Res.* 86, 17–24.
- Li, Q.L., Mahendra, S., Lyon, D.Y., Brunet, L., Liga, M.V., Li, D., Alvarez, P.J.J., 2008. Antimicrobial nanomaterials for water disinfection and microbial control: potential applications and implications. *Water Res.* 42, 4591–4602.
- Li, Y., Zhao, J., Zhang, G.S., Zhang, L.L., Ding, S.Y., Shang, E.X., Xia, X.H., 2019. Visible-light-driven photocatalytic disinfection mechanism of Pb-BiFeO₃/rGO photocatalyst. *Water Res.* 161, 251–261.
- Liang, J.L., Deng, J., Liu, F.Y., Li, M.A., Tong, M.P., 2018. Enhanced bacterial disinfection by Bi₂MoO₆-AgBr under visible light irradiation. *Colloids Surf. B Biointerfaces* 161, 528–536.
- Liu, L.D., Liu, Q., Wang, Y., Huang, J., Wang, W.J., Duan, L., Yang, X., Yu, X.Y., Han, X., Liu, N., 2019a. Nonradical activation of peroxydisulfate promoted by oxygen vacancy-laden NiO for catalytic phenol oxidative polymerization. *Appl. Catal. B Environ.* 254, 166–173.
- Liu, X.D., Tian, J.F., Li, Y.Y., Sun, N.F., Mi, S., Xie, Y., Chen, Z.Y., 2019b. Enhanced dyes adsorption from wastewater via Fe₃O₄ nanoparticles functionalized activated carbon. *J. Hazard Mater.* 373, 397–407.
- Ma, S.L., Zhan, S.H., Jia, Y.N., Shi, Q., Zhou, Q.X., 2016. Enhanced disinfection application of Ag-modified g-C₃N₄ composite under visible light. *Appl. Catal. B Environ.* 186, 77–87.
- McGuigan, K.G., Conroy, R.M., Mosler, H.J., du Preez, M., Ubomba-Jaswa, E., Fernandez-Ibanez, P., 2012. Solar water disinfection (SODIS): a review from bench-top to roof-top. *J. Hazard Mater.* 235, 29–46.
- Michael-Kordatou, I., Iacovou, M., Frontistis, Z., Hapeshi, E., Dionysiou, D.D., Fatta-Kassinos, D., 2015. Erythromycin oxidation and ERY-resistant *Escherichia coli* inactivation in urban wastewater by sulfate radical-based oxidation process under UV-C irradiation. *Water Res.* 85, 346–358.
- Olmez-Hanci, T., Arslan-Alaton, I., Gurlen, S., Gafarli, I., Khoei, S., Safaltin, S., Ozcelik, D.Y., 2018. Oxidative degradation of Bisphenol A by carbocatalytic activation of persulfate and peroxy-monosulfate with reduced graphene oxide. *J. Hazard Mater.* 360, 141–149.
- Pablos, C., Marugan, J., van Grieken, R., Serrano, E., 2013. Emerging micropollutant oxidation during disinfection processes using UV-C, UV-C/H₂O₂, UV-A/TiO₂ and UV-A/TiO₂/H₂O₂. *Water Res.* 47, 1237–1245.
- Qin, H., Wang, C.M., Dong, Q.Q., Zhang, L., Zhang, X., Ma, Z.Y., Han, Q.R., 2015. Preparation and characterization of magnetic Fe₃O₄-chitosan nanoparticles loaded with isoniazid. *J. Magn. Magn Mater.* 381, 120–126.
- Qin, Y.X., Li, G.Y., Gao, Y.P., Zhang, L.Z., Ok, Y.S., An, T.C., 2018. Persistent free radicals in carbon-based materials on transformation of refractory organic contaminants (ROCs) in water: a critical review. *Water Res.* 137, 130–143.
- Rastogi, A., Ai-Abad, S.R., Dionysiou, D.D., 2009. Sulfate radical-based ferrous-peroxy-monosulfate oxidative system for PCBs degradation in aqueous and sediment systems. *Appl. Catal. B Environ.* 85, 171–179.
- Rehman, F., Sayed, M., Khan, J.A., Shah, N.S., Khan, H.M., Dionysiou, D.D., 2018. Oxidative removal of brilliant green by UV/S₂O₈²⁻, UV/HSO₅⁻ and UV/H₂O₂

- processes in aqueous media: a comparative study. *J. Hazard Mater.* 357, 506–514.
- Ribao, P., Corredor, J., Rivero, M.J., Ortiz, I., 2019. Role of reactive oxygen species on the activity of noble metal-doped TiO₂ photocatalysts. *J. Hazard Mater.* 372, 45–51.
- Sun, H.W., Li, G.Y., Nie, X., Shi, H.X., Wong, P.K., Zhao, H.J., An, T.C., 2014. Systematic approach to in-depth understanding of photoelectrocatalytic bacterial inactivation mechanisms by tracking the decomposed building blocks. *Environ. Sci. Technol.* 48, 9412–9419.
- Waclawek, S., Lutze, H.V., Grubel, K., Padil, V.V.T., Cernik, M., Dionysiou, D.D., 2017. Chemistry of persulfates in water and wastewater treatment: a review. *Chem. Eng. J.* 330, 44–62.
- Wang, R., Zhang, W.T., Zhu, W.X., Yan, L.Z., Li, S.H., Chen, K., Hu, N., Suo, Y.R., Wang, J.L., 2018a. Enhanced visible-light-driven photocatalytic sterilization of tungsten trioxide by surface-engineering oxygen vacancy and carbon matrix. *Chem. Eng. J.* 348, 292–300.
- Wang, W.J., Huang, G.C., Yu, J.C., Wong, P.K., 2015. Advances in photocatalytic disinfection of bacteria: development of photocatalysts and mechanisms. *J. Environ. Sci.* 34, 232–247.
- Wang, W.J., Zhang, L.Z., An, T.C., Li, G.Y., Yip, H.Y., Wong, P.K., 2011. Comparative study of visible-light-driven photocatalytic mechanisms of dye decolorization and bacterial disinfection by B-Ni-codoped TiO₂ microspheres: the role of different reactive species. *Appl. Catal. B Environ.* 108, 108–116.
- Wang, W.J., Li, G.Y., Xia, D.H., An, T.C., Zhao, H.J., Wong, P.K., 2017. Photocatalytic nanomaterials for solar-driven bacterial inactivation: recent progress and challenges. *Environ. Sci.: Nano* 4, 782–799.
- Wang, W.J., An, T.C., Li, G.Y., Li, Y.C., Yu, J.C., Wong, P.K., 2018b. Free-standing red phosphorous/silver sponge monolith as an efficient and easily recyclable macroscale photocatalyst for organic pollutant degradation under visible light irradiation. *J. Colloid Interface Sci.* 518, 130–139.
- Wang, W.J., Wang, H.N., Li, G.Y., An, T.C., Zhao, H.J., Wong, P.K., 2019. Catalyst-free activation of persulfate by visible light for water disinfection: efficiency and mechanisms. *Water Res.* 157, 106–118.
- Wu, B.D., Yang, M.H., Yin, R., Zhang, S.J., 2017. Applicability of light sources and the inner filter effect in UV/acetylacetone and UV/H₂O₂ processes. *J. Hazard Mater.* 335, 100–107.
- Wu, H., Xu, X.Y., Shi, L., Yin, Y., Zhang, L.C., Wu, Z.T., Duan, X.G., Wang, S.B., Sun, H.Q., 2019. Manganese oxide integrated catalytic ceramic membrane for degradation of organic pollutants using sulfate radicals. *Water Res.* 167, 15.
- Xia, D.H., He, H.J.W., Liu, H.D., Wang, Y.C., Zhang, Q., Li, Y., Lu, A.H., He, C., Wong, P.K., 2018. Persulfate-mediated catalytic and photocatalytic bacterial inactivation by magnetic natural ilmenite. *Appl. Catal. B Environ.* 238, 70–81.
- You, J.H., Guo, Y.Z., Guo, R., Liu, X.W., 2019. A review of visible light-active photocatalysts for water disinfection: features and prospects. *Chem. Eng. J.* 373, 624–641.
- Zhang, L., Wang, W.Z., Zhou, L., Shang, M., Sun, S.M., 2009. Fe₃O₄ coupled BiOCl: a highly efficient magnetic photocatalyst. *Appl. Catal. B Environ.* 90, 458–462.
- Zhang, L.S., Wong, K.H., Yip, H.Y., Hu, C., Yu, J.C., Chan, C.Y., Wong, P.K., 2010. Effective photocatalytic disinfection of *E. coli* K-12 using AgBr-Ag-Bi₂WO₆ nanojunction system irradiated by visible light: the role of diffusing hydroxyl radicals. *Environ. Sci. Technol.* 44, 1392–1398.
- Zhang, Y.Q., Tran, H.P., Du, X.D., Hussain, I., Huang, S.B., Zhou, S.Q., Wen, W., 2017. Efficient pyrite activating persulfate process for degradation of p-chloroaniline in aqueous systems: a mechanistic study. *Chem. Eng. J.* 308, 1112–1119.
- Zhu, X.D., Liu, Y.C., Luo, G., Qian, F., Zhang, S.C., Chen, J.M., 2014. Facile fabrication of magnetic carbon composites from hydrochar via simultaneous activation and magnetization for triclosan adsorption. *Environ. Sci. Technol.* 48, 5840–5848.
- Zhu, X.D., Qian, F., Liu, Y.C., Matera, D., Wu, G., Zhang, S.C., Chen, J.M., 2016. Controllable synthesis of magnetic carbon composites with high porosity and strong acid resistance from hydrochar for efficient removal of organic pollutants: an overlooked influence. *Carbon* 99, 338–347.